Adaptive Landing Gear: optimum control strategy and improvement potential[1]

Lukasz Jankowski, Grzegorz Mikulowski
Smart Technology Centre, Institute for Fundamental Technological Research
ul. Swietokrzyska 21, 00-049 Warszawa, Poland
E-Mail: (*lukasz.jankowski | grzegorz.mikulowski)@ippt.gov.pl*

Abstract
An adaptive landing gear (ALG), as considered in this paper, is a landing gear (LG) capable of active adaptation to particular landing conditions by means of controlled hydraulic force. The objective of the adaptive control is to mitigate the peak force transferred to the aircraft structure during touchdown, and thus to limit the structural fatigue factor. The paper investigates two control strategies (semi-active and active) and the potential for improvement. As a reference a standard, passive landing gear is considered (nose LG, I23 aircraft, Institute of Aviation, Warsaw, Poland) and the calculated results are evaluated statistically, in terms of the mean and the median peak strut force. Additionally, a general strategy of rebound height mitigation is proposed. Accuracy of the model is verified by comparison of simulations with measurements taken during laboratory test of the reference landing gear. The concept has been verified experimentally using a laboratory test stand.

1 Introduction

The attention in this paper is paid to the control strategies and potential for peak force mitigation, hence the construction details of an active LG head and of all necessary sensors are skipped. The hydraulic force is assumed here to be controlled directly by the orifice area, which in practical implementations can be related to the driving current (magnetorheological head) or voltage (piezovalve solution).

The potential of improvement of an ALG is discussed at two basic LG control strategies:

- semi-active (orifice area fixed before each touchdown and constant during the process),
- active (orifice area actively modified during touchdown).

All landing scenarios considered are based on real data related to the passive version of the nose landing gear, I23 aircraft [1].

Part 2 of the paper states equations of motions and basic parameters. Part 3 discusses in detail the control strategies used to minimise the peak strut force. Part 4 considers mitigation of the rebound height, while Part 5 validates the model against measurement data. Statistical evaluation of improvement potential of an adaptive LG, is presented in Part 6. Part 7 reports on laboratory test stand and experimental verification.

2 Equations of motion

For the purposes of this analysis the (A)LG is represented by a 2-DOF system and modelled with a slightly modified set of equations derived by Milwitzky and Cook [2]:

$$\begin{aligned} m_1\ddot{z}_1 &= m_1 g - F_S - mgL, & z_1(0) &= z_2(0) = 0, \\ m_2\ddot{z}_2 &= m_2 g + F_S - F_G, & \dot{z}_1(0) &= \dot{z}_2(0) = v_{0,} \end{aligned} \tag{1}$$

1 *to appear in: Proc. of the Int. Conf. on Noise & Vibration Engineering, ISMA, 18 – 20 September, Leuven, Belgium, 2006.*

where the following symbols have been used:

z_1, z_2	vertical displacements of upper and lower masses (aircraft and wheel) from initial contact;
g	gravitational constant: g = 9.81 m/s^2;
m, m_1, m_2	total, upper and lower masses: $m = m_1+m_2$, m_2 = 8.71 kg;
L	lift factor, L = 0.667 [3,4];
F_G	vertical force acting on tire at ground;
F_S	total axial strut force;
v_0	initial landing sinking speed.

A schematic diagram of the forces acting in the LG is shown in Fig. 1.

The total mass m and sinking speed v_0 are limited by

$$288\ kg \leqslant m \leqslant 422\ kg, \qquad v_0 \leqslant 2.93\ m/s \quad [3,4]. \tag{2}$$

For detailed statistics of the mass m and sinking speed v_0 see Part 6. Notice that m is the mass per nose landing gear only, i.e. it is less than the total landing mass of the aircraft. 422 kg corresponds to the maximum I23 design landing mass of 1117 kg [1,3] and 282 kg was chosen to be proportional to the mass of an empty aircraft with a pilot.

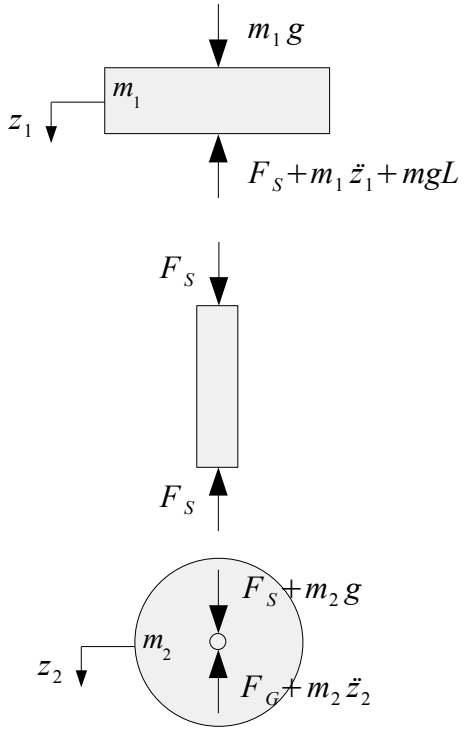

Fig. 1 Schematic diagram of forces acting in landing gear

2.1 Tire characteristics

The dynamic force-deflection characteristics of the I23 nose LG tire has been obtained by fitting experimental data measured in three dynamic tests [3]. The least-square fit is a fourth-order polynomial:

$$F_G(z_2) \approx (7.3\,10^4 + 5.4\,10^6 z_2 - 8.6\,10^7 z_2^2 + 6.4\,10^8 z_2^3) \cdot max(z_2, 0), \tag{3}$$

where the last multiplier denotes symbolically that F_G obviously vanishes when the tire hovers above the ground. The experimental data and the calculated fit are shown in Fig. 2.

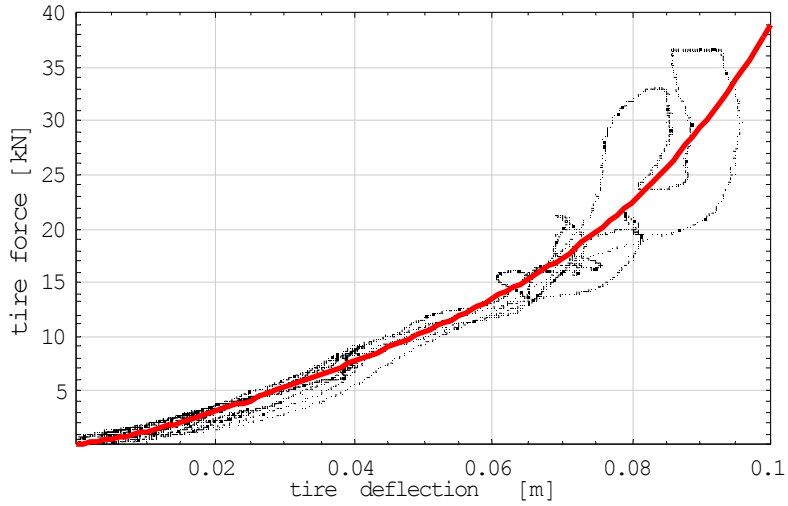

Fig. 2 Measured (dotted) and fitted (continuous) tire force-deflection characteristics (I23 nose LG)

2.2 Total axial strut force

The total axial strut force F_S is modelled as a sum of four forces:

$$F_S = F_a + F_h + F_d + F_f, \tag{4}$$

which are:

F_a pneumatic force in strut (Part 2.2.1);
F_h hydraulic force in strut (Part 2.2.2);
F_d delimiting force to prevent excessive strut elongation (Part 2.2.3);
F_f friction force (Part 2.2.4).

Notice that the introduction of the (actually occurring) delimiting force F_d greatly simplifies modelling of the landing process compared to [2]: the LG can be uniformly modelled as a 2-DOF system thorough the whole landing, including rebounds.

2.2.1 Pneumatic force

The pneumatic force F_a is modelled in accordance with the polytropic law for compression of gases:

$$F_a(s) = p_0 A_a \left(\frac{V_0}{V_0 - s A_a} \right)^n, \tag{5}$$

where the following symbols have been used:

p_0 initial air pressure in the upper chamber of (fully elongated) strut: p_0 = 1.028 MPa;
A_a pneumatic area: $A_a = \pi\ 0.042^2\ \text{m}^2 = 5.542\ 10^{-3}\ \text{m}^2$ [1,3];
V_0 initial air volume of (fully elongated) strut: $V_0 = 171\ 10^{-6}\ \text{m}^3$;
s strut axial stroke: $s = z_1 - z_2$;
n polytropic exponent for air compression process in strut: n = 1.1 [2].

The numerical values of p_0 = 1.028 MPa and $v_0 = 171\ 10^{-6}\ \text{m}^3$ have been obtained by numerical fitting of LG quasi-static compression data [3].

2.2.2 Hydraulic force

The hydraulic force F_h is modelled in the standard way [2] by the equation

$$F_h(\dot{s}) = sign(\dot{s}) \frac{1}{2} \frac{\rho A_h^3}{C_d^2 A_o^2} \dot{s}^2, \tag{6}$$

where the following symbols have been used:

s strut axial stroke: $s = z_1 - z_2$;
ρ density of hydraulic fluid: $\rho = 872.6\ \text{kg/m}^3$ for Aeroshell 41 [5];
A_h hydraulic area: $A_h = \pi\ 0.036^2\ \text{m}^2 = 4.072\ 10^{-3}\ \text{m}^2$ [1,3];
A_o cross-sectional area of discharge orifice: $1\ \text{mm}^2 = A^2_{o(min)} <= A_o <= A^2_{o(max)} = 30\ \text{mm}^2$;
C_d orifice discharge coefficient: C_d = 0.6 [5].

The limits of A_o (the control parameter) are chosen here arbitrarily to model real technological constraints.

2.2.3 Delimiting force

The delimiting force F_d prevents excessive elongation of the strut and attempts to model the actual force occurring on the strut delimiter. It acts only within the last 0.5 mm of the fully elongated strut and is

modelled by a simple spring force:

$$F_d(s) = p_0 A_a \cdot min\left(\frac{s - l_d}{l_d}, 0\right), \tag{7}$$

where the following symbols have been used:
s strut axial stroke: $s = z_1 - z_2$;
l_d delimiting force acting interval: $l_d = 500\ 10^{-6}$ m.

The coefficient $p_0 A_a$ has been chosen to obtain equilibrium at full elongation, i.e. $F_d(0) + F_a(0) = 0$. Notice that possible oscillations of a fully elongated strut will be damped directly by the hydraulic force F_h, thus there is no need for an additional damping term.

2.2.4 Friction force

It is assumed that the friction occurring in the strut is a dry friction only [2,3] and can be modelled by

$$F_f(\dot{s}) = C_f \frac{2}{\pi} \arctan(10^4 \dot{s}), \tag{8}$$

where the following symbols have been used:
s strut axial stroke: $s = z_1 - z_2$;
C_f dry friction coefficient: $C_f = 559$ N.

The inverse tangent function was used to assure smooth variations of the friction force at turning points and thus to enable numerical integrations of the equations of motion. The numerical value of the dry friction coefficient C_f has been obtained by numerical fitting of the LG quasi-static compression data [3]. Notice that the following simplifying assumptions have been made:

- The dynamic friction equals the quasi-static friction.
- The strut friction F_f is not considerably affected by the normal loading occurring at the wheel axle in first milliseconds of the landing process due to tire friction. This is an oversimplification in the case of cantilever-type LG but can be legitimate in the case of levered trailing arm gears.

3 Peak force mitigation

The landing scenario of the LG model stated in Part 2 is fully defined by two parameters:
- total mass m and
- initial landing sinking velocity v_0.

Their ranges are stated in Eq. (2), their distributions in Part 6. The evolution of the strut force F_S and the peak force occurring in each particular landing scenario is hence determined by the area A_o of the discharge orifice. There are essentially three control strategies possible:

- *Passive LG*, i.e. no control: the orifice area A_o is constant and cannot be adjusted to particular landing conditions. Nevertheless, its pre-set constant value is optimised to mitigate the peak strut force occurring at harshest landing conditions (max. design landing mass and max. sinking speed).
- *Semi-active LG*: the orifice area A_o is optimally set directly before each touchdown based on actual sinking velocity and mass. It remains constant during the whole landing process.
- *Active LG*: the orifice area A_o changes continuously during the touchdown according to a set of precomputed scenarios or to an on-line control.

Notice that the above-mentioned strategies apply to the strut compression phase only. During the decompression the recoil orifices take effect instead of the main discharge orifice. Recoil orifice area can also be optimised in order to minimise the rebound effects, which in the passive case is covered by Part 4.

3.1 Passive LG

The pre-set, constant discharge orifice area A_o has to be chosen to minimise the peak force occurring during the harshest-possible design landing scenario, i.e. at m = 422 kg and v_0 = 2.93 m/s.

Fig. 3 shows the calculated dependence of the peak strut force on the discharge orifice area A_o. The left slope corresponds to the decreasing hydraulic force peak, while the right slope corresponds to the increasing pneumatic force peak. The minimum value of 17 022 N has been found at A_o = 17.43 mm^2, at which both peaks are equal. The corresponding computed tire peak force equals 17 374 N, which is relatively very close to the measured value of 17 400 N [3].

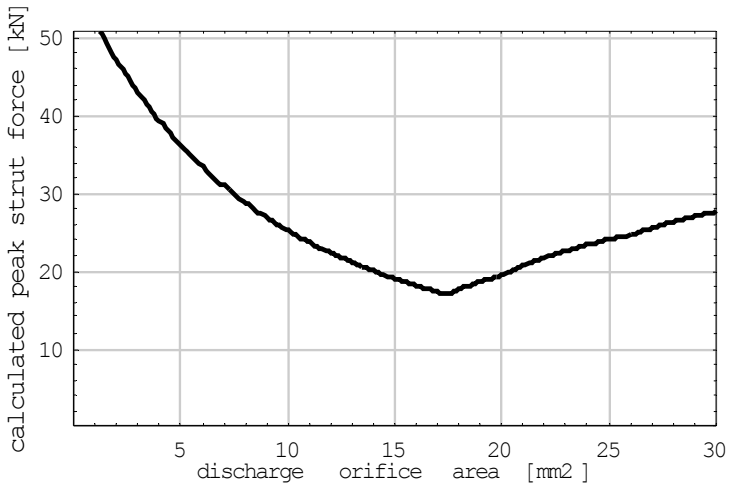

Fig. 3 Passive LG: Calculated dependence of peak strut force on discharge orifice area A_o at harshest design landing scenario (m = 422 kg and v_0 = 2.93 m/s)

Thus, the maximum design strut force was assumed to equal F_{max} = 17 022 N. The optimum discharge orifice area for a passive LG is $A_{o(passive)}$ = 17.43 mm^2.

$$F_{max} = 17022\ N, \qquad A_{o\,(passive)} = 17.43\ mm^2. \tag{9}$$

Fig. 4 presents calculated peak strut force in the optimised passive LG (i.e. at A_o = 17.43 mm2) as a function of the sinking velocity v_0 and the total landing mass m.

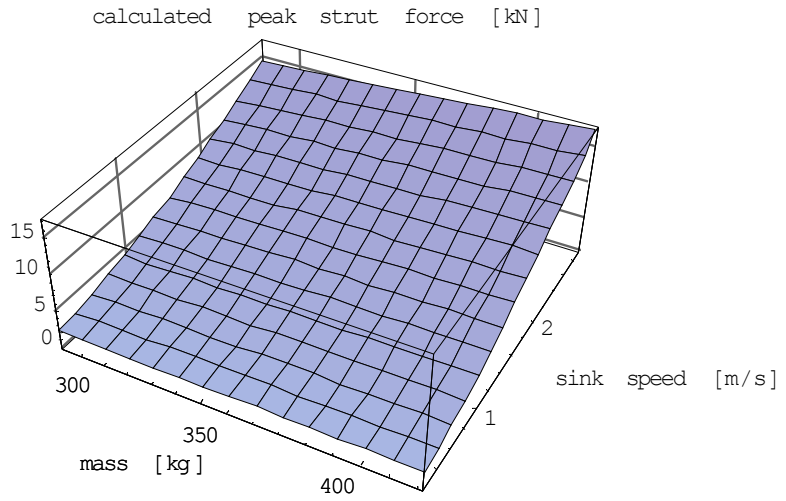

Fig. 4 Passive LG: Calculated dependence of peak strut force on total mass m and sinking speed v_0

3.2 Semi-active LG

The orifice area A_o can be set before each touchdown and stays constant during the whole process. Thus, it can be optimised for each particular landing scenario (defined by a pair (m, v_0)) by minimising the corresponding peak force curve. This is substantially advantageous to the passive LG, which is optimised for the harshest design landing conditions only.

For each landing mass m two curves can be drawn in the (v_0, A_o) coordinate system to illustrate peak strut force optimisation constraints (Fig. 5):

- A line marking the maximum allowed values of the sinking velocity v_0 as a function of the discharge orifice area A_o, drawn in bold lines in Fig. 5. The line is defined by the condition $F_{peak} = F_{max}$ (see Eq. (9)) and separates allowed ($F_{peak} <= F_{max}$) from forbidden ($F_{peak} > F_{max}$) landing characteristics at the considered landing mass m.
- A line marking the optimum values of the discharge orifice area A_o as a function of the sinking velocity v_0, drawn in thin lines in Fig. 5.

Fig. 5 shows the above-mentioned lines drawn for three landing masses. Notice that at lower landing mass the maximum design sinking speed v_0 can be safely exceeded without exposing the strut to the maximum design strut force F_{max}, provided the semi-active strut is optimally controlled. E.g. at the minimum landing mass m = 282 kg F_{max} is attained first at v_0 = 3.67 m/s.

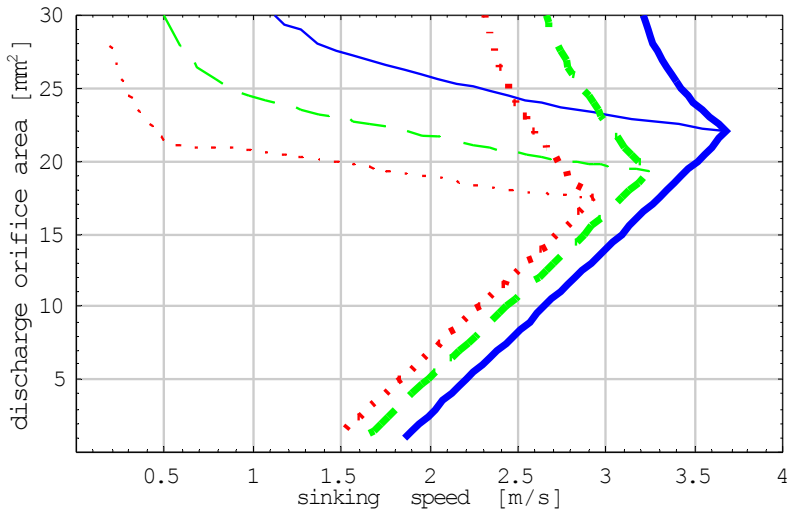

Fig. 5 Semi-active LG: peak strut force optimisation constraints at three landing masses:
282 kg (continuous blue), 352 kg (dashed green), 422 kg (dotted red):
bold lines – maximum design strut force F_{max} attained;
thin lines – optimum values of discharge orifice area A_o

Fig. 6 shows calculated optimum values of the discharge orifice area A_o as a function of the touchdown conditions. Notice that for standard landing conditions (low sinking speed) the optimum orifice area considerably exceeds 17.43 mm^2, which is the value used in the passive LG, optimised for the harshest conditions only. Hence, the peak strut force in the semi-active LG can be expected to be considerably lower than in the passive LG at the same landing conditions. The relative improvement is shown in Fig. 7.

3.3 Active LG

In an actively controlled LG the discharge orifice area A_o is actively modified during strut compression phase. The equations in Part 2.2 directly relate the strut force F_S to the discharge orifice area A_o:

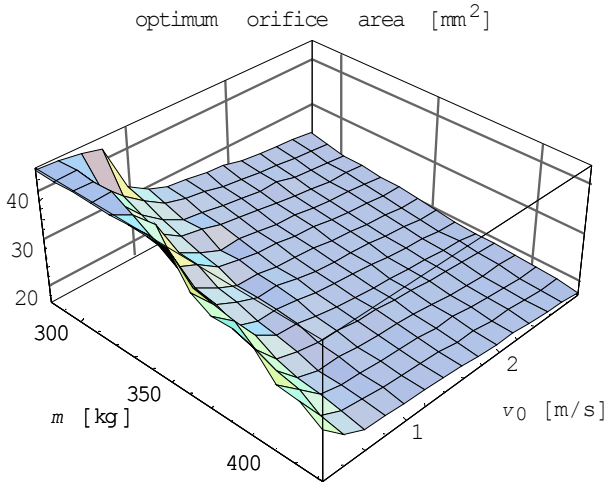

Fig. 6 Semi-active LG: Calculated dependence of optimum value of discharge orifice area A_o on total mass m and sinking speed v_0

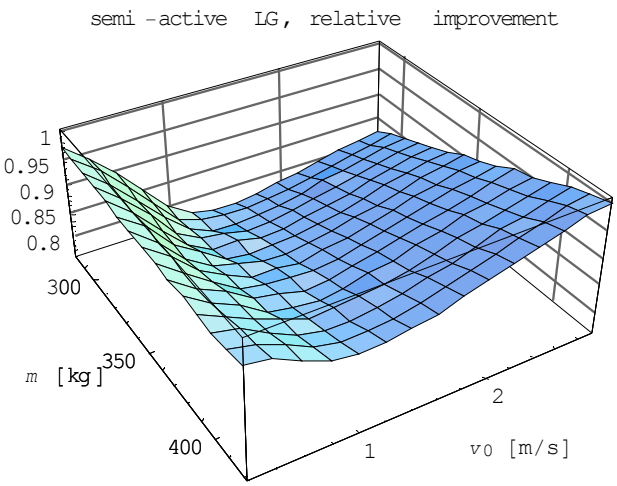

Fig. 7 Semi-active LG compared to passive LG: Calculated ratio of peak strut force in optimally controlled semi-active LG and in passive LG in dependence on total mass m and sinking speed v_0

$$F_S = F_a + F_d + F_f + sign(\dot{s})\frac{1}{2}\frac{\rho A_h^3}{C_d^2 A_o^2}\dot{s}^2. \tag{10}$$

Hence the desired strut force limit $F_{S(limit)}$ can be attained, if possible, by actively setting A_o during the compression phase as follows

$$A_o^2 = max\left(A_{o(min)}^2, min\left(A_{o(max)}^2, \dot{s}^2\frac{\rho}{2}\frac{A_h^3}{C_d^2}\frac{sign(\dot{s})}{F_{S(limit)} - F_a - F_d - F_f}\right)\right), \tag{11}$$

where the functions min and max have been used to confine A_o to the technologically imposed upper and lower limits $A_{o(min)}$ ... $A_{o(max)}$. Notice that, according to Eq. (11), at the very beginning of the strut motion A_o will be set to $A_{o(min)}$ and stay so till F_S attains the desired value of $F_{S(limit)}$. Thereafter A_o will be actively controlled within the given limits until the decompression phase begins.

Basically, the active approach of Eq. (11) require optimisation of the peak force with respect to only one parameter $F_{S(limit)}$, and has to be performed for each landing conditions defined by a pair of (m, v_0). However, it was found that it is advantageous to set the initial value of the discharge orifice area $A_{o(ini)}$ independently of Eq. (11) and begin the active control of Eq. (11) first when the desired force limit $F_{S(limit)}$ is attained. This results in optimisation with respect to two parameters:

- Initial area of the discharge orifice $A_{o(ini)}$.
- Desired strut force limit $F_{S(limit)}$,which triggers and controls the active-control phase.

Their computed optimum values in dependence on the landing conditions are shown in Fig. 8.

Fig. 9 shows the relative improvement in comparison to the semi-active LG, i.e. the ratio of the peak strut force in the optimally controlled active LG to the peak strut force in the optimally controlled semi-active LG. Notice that it is an additional improvement, which should be multiplied by the improvement of the semi-active LG (Fig. 7) to obtain the total improvement to the passive LG.

The improvement at standard landing conditions (i.e. low sinking speed) amounts to 1 % - 2 % only and is rather insignificant. However, at the harshest landing conditions (max. mass and max. sinking velocity) it attains the maximum of approx. 6 %, which is in contrast to the semi-active strategy (no improvement). Statistical performance is discussed in Part 6.

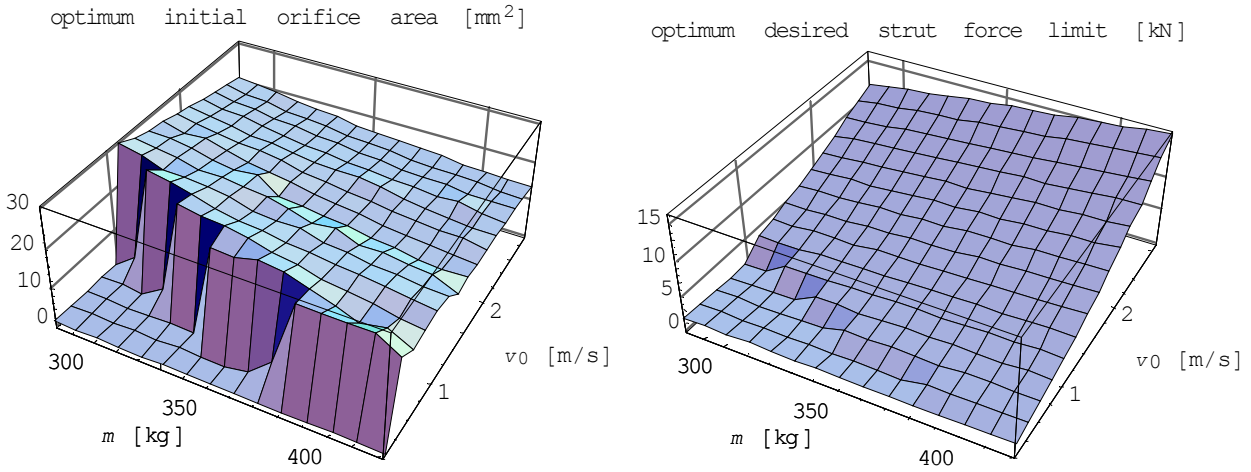

Fig. 8 Active LG: Calculated dependence of optimum value of:
(left) initial discharge orifice area $A_{o(ini)}$; (right) desired strut force limit $F_{S(limit)}$;
on total mass m and sinking speed v_0

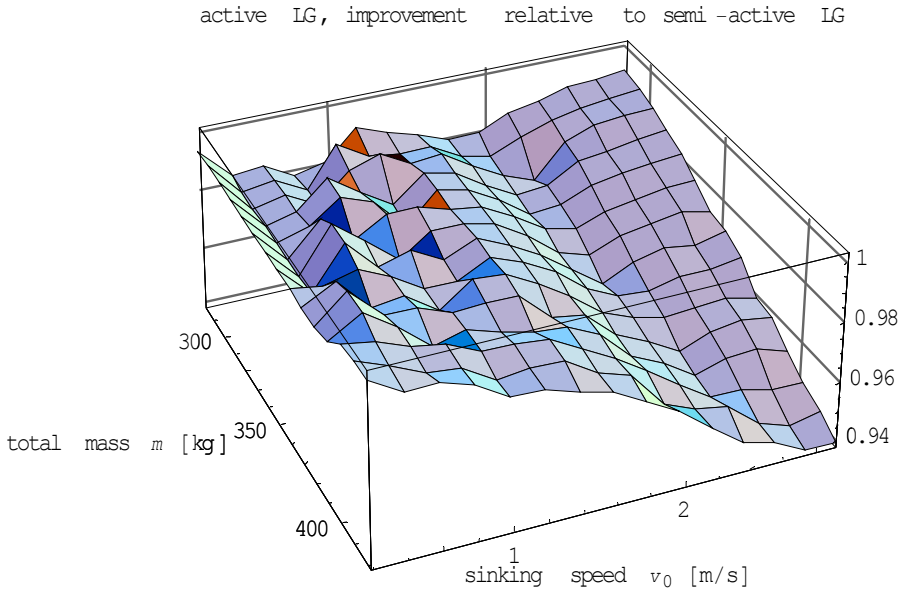

Fig. 9 Active LG compared to semi-active LG:
Calculated ratio of peak strut force in optimally controlled active LG and semi-active LG
in dependence on total mass m and sinking velocity v_0

4 Rebound mitigation

The control strategies discussed in Part 3 apply to the strut compression phase only and are designed to minimise the peak strut force transferred to the aircraft structure. During the decompression phase the recoil orifices take effect and the rebound behaviour of the LG becomes crucial. This paper assumes the recoil orifice area to be constant and discusses its passive optimisation with the goal of minimising the expected rebound height, i.e. the following objective function:

$$\int_0^{V_{max}} \int_{M_{min}}^{M_{max}} f(v_0, m)\, R_h(v_0, m)\, dm\, dv_0, \tag{12}$$

where the following symbols have been used:

v_{max} maximum initial landing sinking speed: v_{max} = 2.93 m/s, Eq. (2);
M_{min}, M_{max} minimum and maximum total landing mass: M_{min} = 282 kg, M_{max} = 422 kg, Eq. (2);
$f(v_0, m)$ probability density function (pdf) of landing condition distribution, see Part 6;
$R_h(v_0, m)$ wheel rebound height calculated at a given LG control scheme.

Computed expected rebound heights for three considered LG (passive, semi-active and active) in dependence on the recoil orifice area are shown in Fig. 10. Table 1 lists the optimum values of $A_{o(rev)}$.

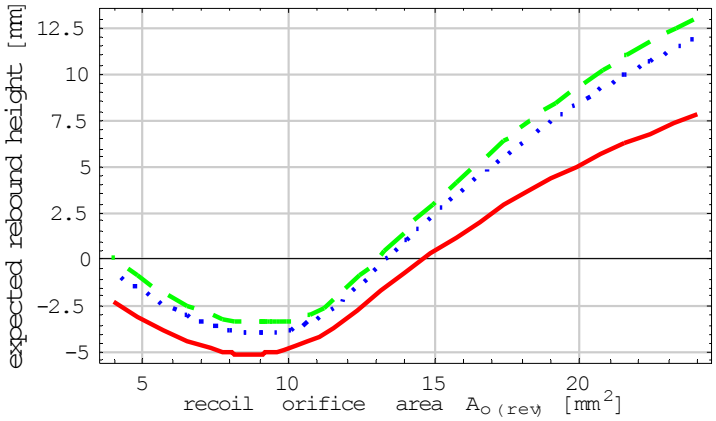

Fig. 10 Calculated expected rebound heights in dependence on the recoil orifice area: passive LG (continuous), semi-active LG (dashed), active LG (dotted)

LG type	optimum recoil orifice area $A_{o(rev)}$ [mm^2]
passive	8.7
semi-active	9.1
active	9.0

Table 1 Calculated optimum recoil orifice area $A_{o\,(rev)}$

Notice that the peak strut force occurs during the compression phase, hence the recoil orifice area $A_{o\,(rev)}$, which affects the decompression phase, could be optimised independently of the main orifice area A_o. The probability density functions of the touchdown conditions and the objective function of Eq. (12) have been discretised for the purpose of the calculations to reflect the discrete independent landing statistics (Part 6).

5 Comparison with measurements

Accuracy of the model can be partly verified by comparison of calculated forces and displacements with the forces and displacements measured in tests of a real I23 nose LG, passive version. Institute of Aviation (Warsaw, Poland) has made available two sets of measurement data suitable for such a comparison [3]:

- total mass m = 422 kg, sinking velocity v_0 = 2.93 m/s, lift factor L = 0.667;
- total mass m = 422 kg, sinking velocity v_0 = 3.52 m/s, lift factor L = 1.

Notice that the first case corresponds to the harshest design landing conditions, while the second is even more demanding. Fig. 11 compare calculated and measured tire forces F_G, while Fig. 12 compare calculated and measured aircraft and tire displacements.

Simulations and measurements agree well in the case of

- the tire force F_G;
- the first 150 ms of tire displacements;
- the first 100 ms of aircraft displacements, which correspond to the strut compression phase.

However, there is an increasing discrepancy between the displacements calculated and measured in the strut decompression phase, which starts approx. 100 ms after the impact. The discrepancy suggests additional factors coming into play during the strut decompression phase, which cannot be thus modelled using a constant recoil orifice area, as it has been done in Part 4. Nevertheless, the strut compression phase seems to be modelled reliably, hence all the considerations of this paper concerning the peak strut force and the proposed control strategies are valid.

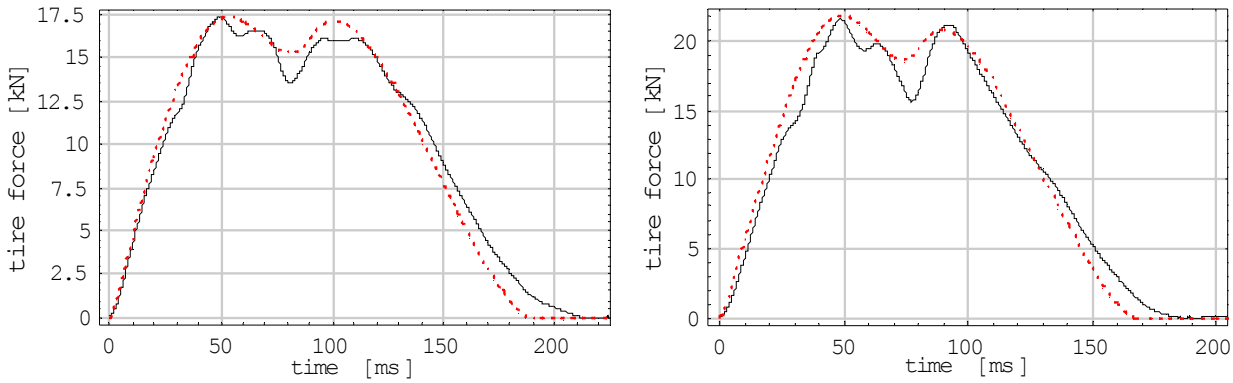

Fig. 10 Calculated (dotted red) and measured (continuous black) tire force F_G, passive LG, m = 422 kg: (left) v_0 = 2.93 m/s, L = 0.667; (right) v_0 = 3.52 m/s, L = 1

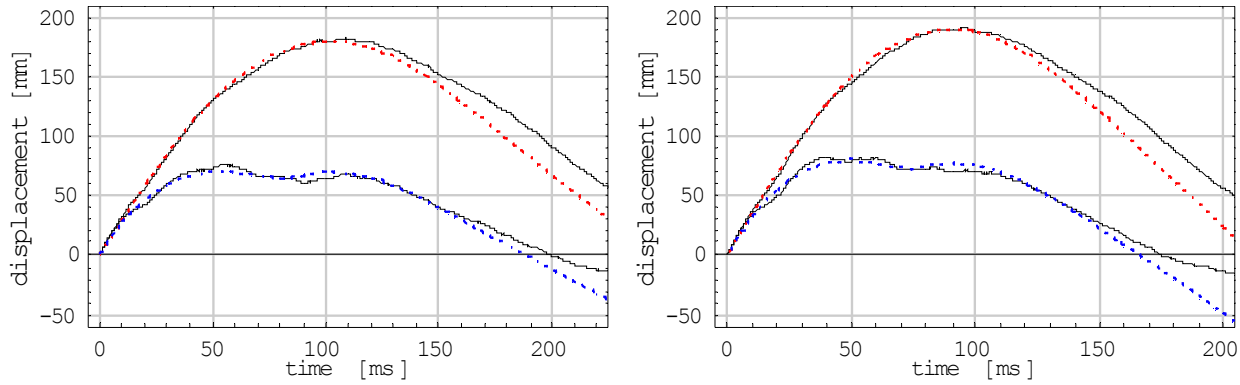

Fig. 11 Calculated (dotted) and measured (continuous black) aircraft and tire displacements, passive LG, m = 422 kg: (left) v_0 = 2.93 m/s, L = 0.667; (right) v_0 = 3.52 m/s, L = 1

6 Potential for improvement

Fig. 7 and Fig. 9 compare the performance of the discussed LG types for each design landing conditions separately. An overall comparison is possible by statistical means (Table 3), if the probability distributions of landing conditions are defined.

The initial sinking velocity v_0 and the total mass m are assumed to be independent. To ease the statistical computations their ranges have been discretised into 15 equally spaced values (0.195 m/s and 10 kg each, respectively). The distribution of the landing mass m has been assumed to be uniform in the whole interval 282 kg to 422 kg, which leads to 66.67 occurences per 1000 landings in each subinterval. The assumed distribution of the initial sinking velocity v_0 is listed in Table 2 (cumulative occurrences) and illustrated in Fig. 13 (occurrences).

Notice that a negative rebound height means the wheel stays in touch with the ground, i.e. no rebound.

Interval No	1	2	3	4	5	6	7	8	9	10	11	12	13	14	15
Sinking speed v_0 [m/s]	0.20	0.39	0.59	0.78	1.00	1.17	1.37	1.56	1.76	1.95	2.15	2.34	2.54	2.74	2.93
Cumulative occurrences	1000	900	730	530	350	210	115	55	25	11	5	2.4	1.2	0.6	0.25

Table 2 Assumed cumulative occurrences of sinking velocities per 1000 landings

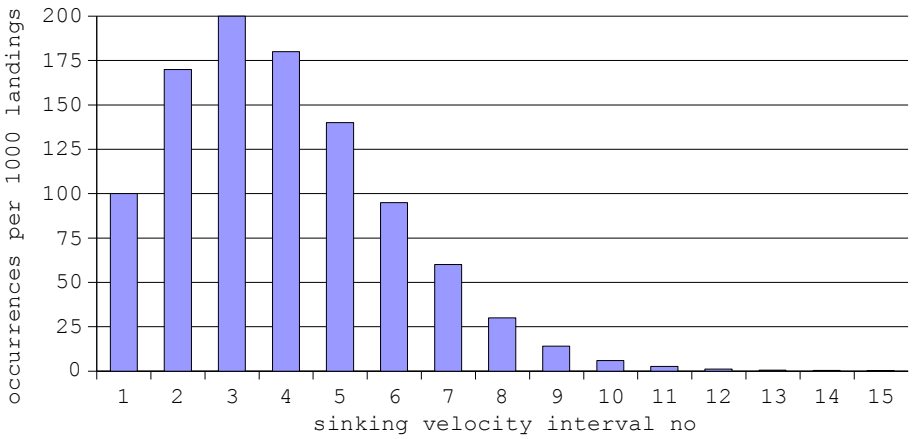

Fig. 13 Assumed occurrences of sinking velocities per 1000 landings

LG type	peak strut force			wheel rebound height		
	expected value [kN]	median value [kN]	99th percentile [kN]	expected value [mm]	median value [mm]	percent of positive rebounds
passive	3.866	3.560	8.736	-5.1	-6.1	5.5 %
semi-active	3.380	3.000	7.751	-3.4	-5.4	11.5 %
active	3.333	2.974	7.517	-3.9	-5.4	11.5 %

Table 3 Performance of three LG control strategies: a statistical comparison

7 Laboratory verification

The results obtained numerically were experimentally verified in the laboratory. For the testing purposes a laboratory scale demonstrator was developed. It had been designed in a way to reflect the behaviour of the adaptive landing gear. The adaptability of the demonstrator was achieved by means of taking advantage of features of magnetorheological fluid behaviour. The laboratory model contained a magnetorheological damper which was excited by impact loading on the drop test stand. The conditions created for the demonstrator were analogical to the conditions being in use during professional testing of the landing gears prototypes.

The laboratory testing had two main purposes: to prove feasibility of the proposed concept and to assess the potential gain that can be achieved thanks to introduction of the adaptive landing gears. The tests were divided into two stages. During the first stage the model controlled by the semi-active strategy was verified and in the second stage a model with active control strategy was tested.

7.1 Experimental equipment

The tests were performed on a small drop test device developed in the laboratory. The idea behind the stand was to ensure its compatibility with testing stands being in use in large landing gear laboratories conducting tests for aircraft manufacturers. The stand was designed to realize the same phenomena of impact excitation that is used in case of LG testing. In Fig. 14 the views of the developed small lab-scale drop test stand and a large drop test stand are presented. The idea of LG testing in professional laboratories is to fix experimental objects to a drop mass. The mass has weight which is equal to the half weight of the aircraft that the landing gear is designed for (in case of main landing gears). The test procedure includes free falling drops from various heights and measuring the parameters characterizing the landing strut. In

order to make the laboratory landing conditions more close to reality the strut is tested on various attitude angles (0 – 15 degree) and with variable circumferential speed of the wheel. For the purpose of the small lab scale experiment the requirements of the testing procedure were simplified in the following points:

1. The tests were conducted only for the vertical position of the adaptive shock absorber.
2. The tire from the original landing strut was substituted by a bumper made of solid rubber.
3. Having in mind the structure simplification the damping element was not mounted to the falling mass but fixed in the vertical position on the foundation plate.

Fig. 14 Developed lab scale drop test stand (left) and full scale drop test stand (right)

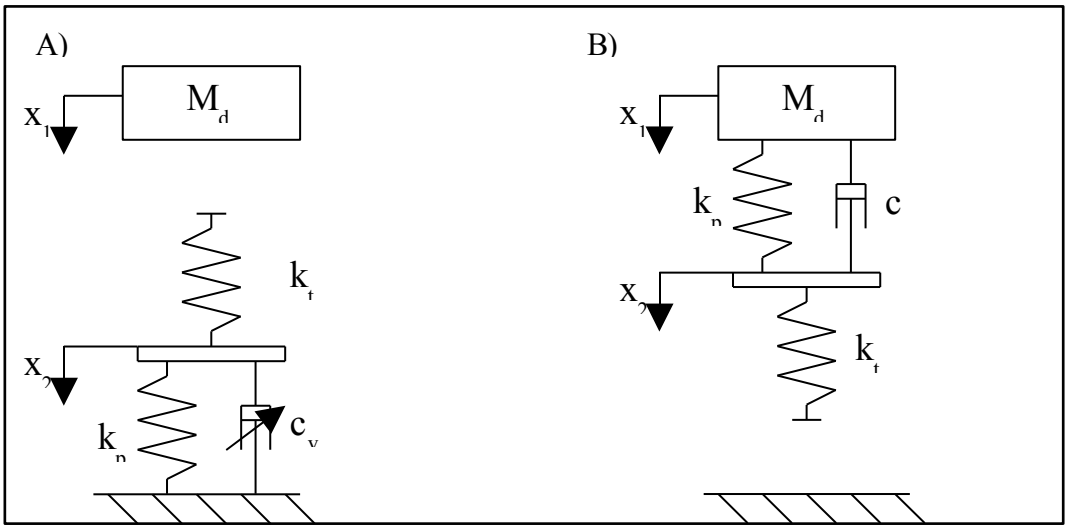

Fig. 15 Comparison of schemes of the lab test stand (A) and a full scale professional test stand (B)

The introduced simplifications caused that during the experiment friction forces generated on the sliding surfaces of the damper were much lower, the introduced rubber element had different characteristic in comparison to characteristic of the tire. However, from mechanical point of view both systems were analogical (Fig. 15) and the effect of the control system could have been successfully tested and assessed.

The main components of the lab scale drop test stand were (Fig. 16) a magnetorheological (MR) damper (1) mounted in a vertical position, a frame and a carriage. The stand was fixed to a foundation plate in order to reduce measurement noise. The lift mechanism enabled to conduct the drop tests up to 700 mm height. In order to ensure the stability of the vertical movement the mass (2) was guided by a rail system embedded in the frame. The impact of the dropped carriage took place via a rubber bumper (3) located on the impact surface.

The following signals were acquired during the tests (Fig. 16): force signal from sensor fixed to a piston rod of the MR damper (4) (measurement of the full impact history), signal from an optical switch (5)

acting as a trigger and enabling determination of the horizontal speed of the carriage just before the impact. The testing procedure covered also measuring of accelerations in two points: deceleration of the falling mass (6a) and acceleration (6b) of the piston rod of the MR damper (7).

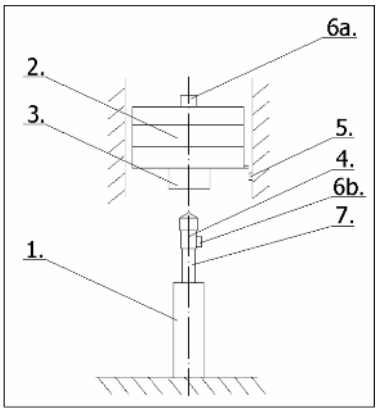

Fig. 16 Lab stand scheme

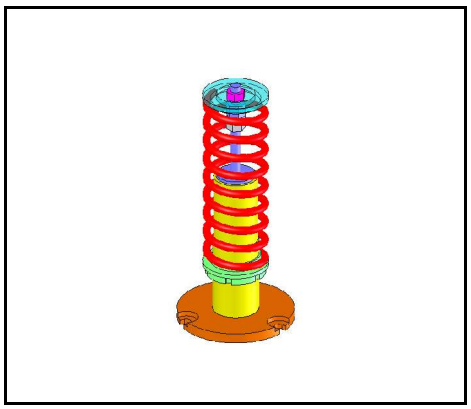

Fig. 17 Adaptive Shock Absorber

The stand described above was used for testing the semi-active control strategy. To test the active control it was supplemented with a linear spring that worked in parallel with the MR damper. Sketch of the tested shock absorber is presented in Fig. 17. The modification in the lab model was introduced in order to change the characteristic of the device and make it more similar to the aircraft LG stiffness characteristics.

7.2 Experimental results of semi active control execution

For testing the semi-active control strategy a special sequence was prepared, which allowed to check the potential of the MR damper as an impact absorbing device. The analysis plan contained a field of impact energies that were to be tested experimentally. The impact energies were chosen to cover an area of possible cases of impacts. The range of the impacts was described by: velocities from 0.5 m/s to 1.67 m/s and masses: 22 kg, 32 kg and 42 kg. The objective of the control was to establish for each of the impact energies a constant control signal level that would ensure that the whole energy was dissipated on a stroke equal 35 mm with the minimal dynamic force induced. The optimal control signal levels were obtained experimentally. In the first step the optimal control was found for the highest energy and taken as a reference value for all other cases, since it is a commonly used practice of design of passive LG. Each conventional passive LG is designed in the way that it is able to withstand the impacts with maximal energies in the optimal way. The whole range of middle energy impacts is dissipated in a non optimal way which causes increase of forces transferred to the aircraft fuselage and increase of their fatigue.

The tests for the lower impact energies were each time conducted in two steps. For the first step a drop was performed with the control signal level optimized for the highest impact energy (reference level) and in the second step the control signal was optimized to the actual impact energy level. The gains in the generated peak force levels are depicted on the diagram in Fig. 18. Two horizontal axes depict impact velocity and mass of the falling body. The vertical axis represents the residual force which reflects the peak force level after adaptation in comparison to the peak force level obtained with the referenced control signal. The diagram proves that introduction of the semi-active control lets to achieve up to 25 % reduction of the dynamic peak force level. The experimental results verify the results obtained numerically. The character of the experimental result is consistent with numerics for the high impact velocities, see Fig. 7. For small impact velocities the results are not similar since the numerical model had implemented a strong pneumatic spring which gives very strong force contribution for the impacts with low initial velocity. The general conclusion is that the principle of the semi-active LG is feasible which was proved in the laboratory experimental tests.

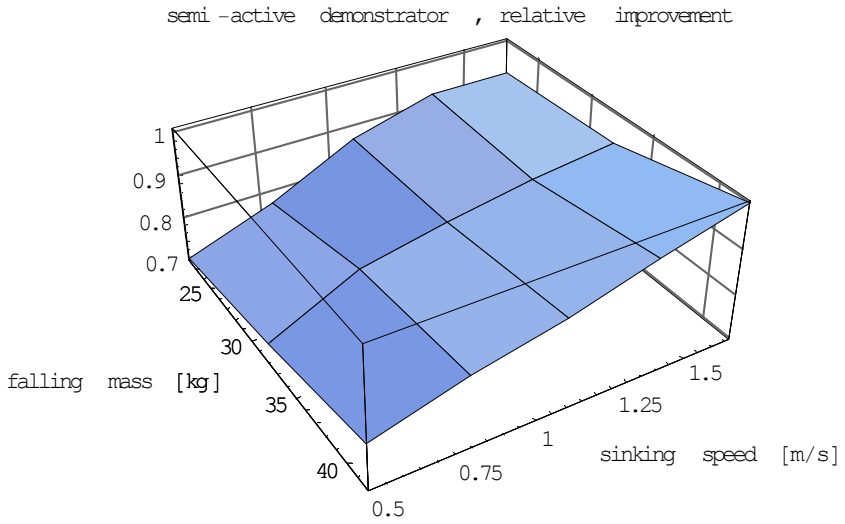

Fig. 18 Semi-active control scheme compared to passive control scheme:
ratio of measured peak forces in optimally controlled semi-active absorber and passive absorber
in dependence on falling mass and sinking speed

7.3 Experimental results of active control execution

The second stage of the experimental verification of the proposed concept was conducting tests with active control strategy. The testing stand was modified by adding a linear spring to the system in order to obtain the behaviour of the model similar to the behaviour of a LG. The linear spring was a substitute for the pneumatic spring used in the conventional designs (Fig. 15). The control system which realized the active control strategy was a feedback loop with monitoring of the dynamic force induced during the impact. The control sequence had three main stages during operation:

1. Recognition of the energy of impact,
2. Adaptation of the system,
3. Execution of the feedback control strategy.

The main objective of the feedback control was to keep the dynamic force on the level determined in accordance to the actual impact energy.

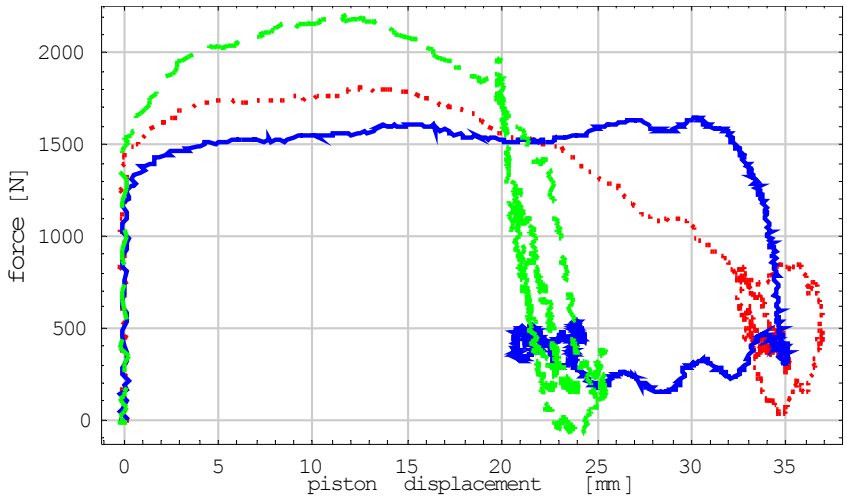

Fig. 18 Measured piston hystereses at three control strategies:
passive (dashed green), semi-active (dotted red) and active (continuous blue)

The results of the control system performance are presented on an example of a series of drop tests performed with mass 54 kg and initial impact velocity 1.37 m/s. The testing series included three drops characterized by the same impact energy (Fig. 19): a reference drop test with the reference control signal (dashed green), an adapted drop case in which the damping force was semi-actively adapted (dotted red) and a drop test during which the active control strategy was executed (continuous blue). An additional assumption for the test was that the maximal stroke of the dissipation can not exceed 35 mm. Fig. 19 presents the comparison of the dynamic forces obtained during the series of experiments in the domain of the piston displacement. The dashed green line, depicting the reference drop result, has the peak force on the level which is 22 % higher than the adapted peak force and 30 % higher than in the case of active energy dissipation.

Conclusions

All simulations in this report have been based on the I23 nose LG, other LG could lead to slightly different numerical results. Nevertheless, the most important findings are clear and can be summarised as follows:

1) The superiority of the adaptive paradigm is clearly confirmed by simulations and laboratory tests. Both modelled adaptive LG excel the modelled passive LG by approx. 16 % in terms of the median peak strut force. Up to 30 % improvement has been obtained in laboratory tests.
2) The improvement between the modelled semi-active and active LG seems to be statistically insignificant (less than 1 % in terms of median peak strut force). However, the advantage of the active LG increases with the sinking velocity and landing mass to attain 6 % at the harshest design landing conditions (at which the semi-active control shows no improvement). Therefore, implementation of active LG control can:
    a) significantly mitigate the peak strut force transferred to the aircraft structure and potential structural damage at most demanding landing conditions (high mass/sinking velocity), which rarely occur but are the most dangerous;
    b) increase the limiting sinking velocity, especially at high landing masses.
3) As the laboratory tests showed much better performance in the active case, the limiting factor seems to be the stiffness of the air spring, which prevents utilisation of the full stroke length. Possibly, the problem could be partially overcome by an air spring with double-stage characteristics and considerably softer first stage. This will be a subject of further investigations.

Acknowledgements

The authors are grateful to Mr. Wojciech Kowalski for measurement data of the I23 nose LG and technical hints [3]. This research was supported by the EU FP6 project ADLAND (IST–FP6–2002–Aero 1-502793–STREP) and the 5FP EU Research Training Network SMART SYSTEMS (HPRN-CT-2002-00284).

References

[1] I23 Technical specification, Institute of Aviation, Warsaw, Poland.

[2] B. Milwitzky, F. E. Cook, *Analysis of Landing Gear Behaviour*, Report 1154, NACA TN 2755, 1952.

[3] Personal communication with Mr. Wojciech Kowalski, Institute of Aviation, Warsaw, 25th Oct. 2005.

[4] FAR Part 23.

[5] D. Batterbee, N. D. Sims, R. Stanway, *ADLAND report: Annex USFD-1(a): Oleo-pneumatic shock absorber modelling and initial MR device sizing*, The University of Sheffield, 2004.